Eur. Phys. J. D (2019) 73: 262
https://doi.org/10.1140/epjd/e2019-100552-2

THE EUROPEAN PHYSICAL JOURNAL D

Regular Article

Strongly resolved diffraction resonances in positronium formation from C_{60} in forward direction*

Paul-Antoine Hervieux[1,a] and Himadri S. Chakraborty[2,b]

[1] Université de Strasbourg, CNRS, Institut de Physique et Chimie des Matériaux de Strasbourg, 67000 Strasbourg, France
[2] Department of Natural Sciences, D.L. Hubbard Center for Innovation, Northwest Missouri State University, Maryville, Missouri 64468, USA

Received 31 October 2019 / Received in final form 21 November 2019
Published online 19 December 2019

Abstract. Positronium formation by capturing from various levels of C_{60} within 10 degrees around the incoming positron direction is calculated. Results indicate dominant strength of the Ps signal and higher resolution of the diffraction resonances, predicted earlier [P.A. Hervieux, A.R. Chakraborty, H.S. Chakraborty, Phys. Rev. A **95**, 020701(R) (2017)], in the forward direction. This raises the possibility of experimental determination of the resonances in angle differential measurements. We further analyze our results by comparing the positron scattering versus positron-electron pairing components of the amplitude for better insights.

1 Introduction

Among inelastic scattering processes of positron impact on both atomic [1] and condensed matter [2], the formation of positron-electron transient bound state, positronium (Ps), is a strong observable channel. There is a range of applied interests in the studies of Ps formation mechanism resulting in electron-positron annihilation [3] in astrophysical [4], materials [5], and pharmaceutical [6] research. Response of antimatter to gravity [7] may use dipositronium molecules [8] and antihydrogen atoms [9] whose production features Ps formation as the maiden step. Other interests include, for instance, the production of Bose–Einstein condensate of Ps [10,11], the role of Ps for diagnostics of porous materials [12] and the test of bound-state quantum electrodynamic theory [13].

The development of the technology for accumulating slow positrons [14] is making it possible to generate high density Ps signals by choosing a diverse range of targets for positron impingement. Such targets include, for instance, gas-phase atoms and molecules [15], polyatomic molecules [16], solids [17], liquids and polymers [18], zeolites [19], metal surfaces and films [20,21], metal-organic frameworks [22,23], and embedded mesostructures [24]. To facilitate precision measurements of gravitational free fall of antimatter as well as of the optical spectrum of Ps, Doppler-corrected Balmer spectroscopy of Rydberg Ps has been applied [25]. Recently high yields of laser assisted production of low-energy excited Ps is achieved in the interaction of cold-trapped positrons with Rydberg excited Cs atom [26].

In spite of such a vast range of target choices, no experiment has yet been published on the Ps formation from vapor phase nanoparticles. On the other hand, the spectroscopic studies of nanoparticles by electron, positron, ion or photon probes can be very interesting in which unique fundamental effects can be unraveled. This is because the finite size electron gas in nanoparticles can underpin diffraction and collective-type resonance effects. One attractive choice of nanoparticle targets for Ps formation may be carbon fullerene molecules which can be abundantly synthesized, are stable and can be sustained in the room temperature environment. The lead theoretical study of Ps formation from C_{60} was published recently by us [27,28]. It has been shown that the formation of a gas of delocalized electrons within a finite nano-region of well defined short-range boundary at the C_{60} shell, in contrast of a long-range Coulombic decay of atomic and molecular electron densities, ensures dominant electron capture from localized regions. This leads to diffraction in the capture amplitude, particularly at positron energies that cannot excite plasmon modes. Indeed, reference [27] revealed a series of diffraction resonances in Ps formation from C_{60} and, more recently, reference [29] demonstrated the shrinking of the resonance structure in energy for a larger C_{240} diffractor.

The hope is that these resonances may be observed in the experiment both in ground and excited state Ps

* Contribution to the Topical Issue "Low-Energy Positron and Positronium Physics and Electron-Molecule Collisions and Swarms (POSMOL 2019)", edited by Michael Brunger, David Cassidy, Saša Dujko, Dragana Maric, Joan Marler, James Sullivan, Juraj Fedor.

[a] e-mail: hervieux@unistra.fr
[b] e-mail: himadri@nwmissouri.edu

formation from fullerenes. But there may still be some roadblocks to accomplish this task within the current laboratory techniques. It may still be a challenge to measure the target-state differential Ps-signals [30] which is vital to capture these resonances well resolved. The technique to measure the recoil momentum of the cations can be improved by using a supersonic gas jet to increase the overlap with the positron beam. On the other hand, resolving the Ps level may not be so critical, since Ps($1s$) signal should largely dominate. Although even this may be accomplished by laser spectroscopy of a dense Ps gas. However, what is demonstrated in the current work is that the measurements within a narrow forward angle of Ps formation can better resolve the resonances without compromising the overall signal strength. The current laboratory technology may be more amenable to angle-differential rather than angle-integrated measurements. For atomic systems, Ps formation in the forward direction was already measured to be the dominant direction [31,32]. Here, we predict such dominance for a fullerene target as well for the first time, and show that even the resonance structures are far pronounced in the forward direction. The following section presents a succinct account of the theoretical formalisms employed. Section 3 presents and discusses the results, while the final section concludes the article. Atomic units are used unless otherwise stated.

2 Brief theoretical account

The details of the methods follow the framework as described in reference [29]. We will present a very brief account of the scheme. The jellium potentials, $V_{\rm jel}(\boldsymbol{r})$, representing 60 C^{4+} ions for C_{60} is constructed by smearing the total positive charge over a spherical shell of radius $r_c = 3.54$ Å (6.7 a.u.) and thickness Δ. A constant pseudopotential V_0 is added to the jellium for quantitative accuracy [33]. The Kohn-Sham equations for systems of 240 electrons, made up of four valence ($2s^2 2p^2$) electrons from each carbon atom, are then solved to obtain the single electron ground state orbitals in the local density approximation (LDA). The parameters $V_0 = 0.445$ a.u. and $\Delta = 1.30$ Å are determined by requiring both charge neutrality and obtaining the experimental value [34] of 7.51 eV of the first ionization thresholds of C_{60}.

Using the single-particle density $\rho(\boldsymbol{r})$ the LDA potential can be written as,

$$V_{\rm LDA}(\boldsymbol{r}) = V_{\rm jel}(\boldsymbol{r}) + \int d\boldsymbol{r}' \frac{\rho(\boldsymbol{r}')}{|\boldsymbol{r} - \boldsymbol{r}'|} + V_{\rm XC}[\rho(\boldsymbol{r})], \quad (1)$$

where the 2nd and 3rd terms on the right are the direct Hartree and the basic exchange-correlation (XC) components. This basic XC functional $V_{\rm XC}$ is parametrized directly from $\rho(\boldsymbol{r})$ by the following formula [35]:

$$V_{\rm XC}[\rho(\boldsymbol{r})] = -\left(\frac{3\rho(\boldsymbol{r})}{\pi}\right)^{1/3} - 0.0333 \log\left[1 + 11.4\left(\frac{4\pi\rho(\boldsymbol{r})}{3}\right)^{1/3}\right], \quad (2)$$

in which the first term on the right is exactly derivable by a variational approach from the HF exchange energy of a uniform electron system with a uniform positively charged background and the second term is the so called correlation potential, a quantity not borne in Hartree–Fock formalism. The XC-functional that utilizes equation (2) is then further refined by adding a parametrized potential [36] in terms of the reduced density and its gradient $\nabla\rho$ as follows,

$$V_{\rm LB} = -\beta[\rho(\boldsymbol{r})]^{1/3} \frac{(\xi X)^2}{1 + 3\beta\xi X \sinh^{-1}(\xi X)}, \quad (3)$$

where $\beta = 0.05$ is empirical and $X = [\nabla\rho]/\rho^{4/3}$. The parameter ξ is a factor arising in transition from the spin-polarized to spin-unpolarized form [37]. Equation (3) is known as the Leeuwen–Baerends (LB) model potential.

C_{60} produced bands of six π (one radial node) and ten σ (nodeless) states. Among these, the HOMO, HOMO-1 levels are of $7h$ ($\ell = 5$) and $6g$ ($\ell = 4$) π character respectively – a result known from the quantum chemical calculations [38] supported by direct and inverse photoemission spectra [39], and from energy-resolved electron-momentum density measurements [40]. The HOMO-2 and HOMO-3 levels are respectively of $10l$ ($\ell = 9$) σ and $5f$ ($\ell = 3$) π character. Linear response type calculations using this ground state basis well explained measured photoemission response of C_{60} at the plasmon excitation energies [41,42]. Similar calculations at higher energies also supported an effective fullerene width accessed in the HOMO and HOMO-1 photoemission experiment [43].

We consider an incoming positron of momentum $\boldsymbol{k}_i$ which captures an electron from a C_{60} bound state $\phi_i(\boldsymbol{r}_-)$ to form a Ps state $\phi_f(\boldsymbol{\rho})$. As illustrated in Figure 2, the positron and electron position vectors, $\boldsymbol{r}_+$ and $\boldsymbol{r}_-$ respectively, originate from the center of the C_{60}^+ ion so that $\boldsymbol{\rho} = \boldsymbol{r}_+ - \boldsymbol{r}_-$ is their relative position vector. $\boldsymbol{k}_{+(-)}$ denote positron (electron) outgoing momenta in Ps that are equal, resulting $\boldsymbol{k}_\beta = 2\boldsymbol{k}_{+(-)}$ to be the momentum of Ps itself. Since by allowing the electron excitation energy to begin from 50 eV we avoid the fullerene plasmon resonances, the many-body effect is not important. In this frame, the prior form of the Ps formation amplitude can be given in the continuum distorted-wave final-state (CDW-FS) approximation [44,45] as,

$$T^-_{\alpha\beta}(\boldsymbol{k}_i) \sim \int d\boldsymbol{r}_- F^{(-)^*}_{\boldsymbol{k}_-}(\boldsymbol{r}_-) W(\boldsymbol{r}_-; \boldsymbol{k}_i) \phi_i(\boldsymbol{r}_-), \quad (4)$$

in which

$$W(\boldsymbol{r}_-; \boldsymbol{k}_i) = \int d\boldsymbol{r}_+ F^{(-)^*}_{\boldsymbol{k}_+}(\boldsymbol{r}_+) \phi^*_f(\boldsymbol{\rho}) \times \left[V^{\rm sc}_i(r_+) - \frac{1}{\rho}\right] F^{(+)}_{\boldsymbol{k}_i}(\boldsymbol{r}_+), \quad (5)$$

where F's are various distorted Coulomb continuum waves.

The positron scattering potential in equation (5) is given by,

$$V^{\rm sc}_i = V^{\rm sr}_i(r_+) + \frac{1}{r_+}, \quad (6)$$

where $V_i^{\rm sr}$ is the short-range part of the positron-residual target interaction associated with the C_{60} orbital labeled i so that

$$V_i^{\rm sr}(r_+) = -V_{\rm jel}(r_+) - \sum_{k=1;k\neq i}^{N_{\rm orb}} V_{\rm H}[\rho_k(\boldsymbol{r})] - \frac{(Z+1)}{r_+}\,, \quad (7)$$

in which $N_{\rm orb}$ is the number of fullerene orbitals, and $V_{\rm H}$ and $V_{\rm jel}$ are respectively the Hartree and the jellium potential as in equation (1).

The initial fullerene orbital is

$$\phi_i(\boldsymbol{r}_-) = R_{n_t\ell_t}(r_-)\, Y_{\ell_t,m_t}(\hat{r}_-), \quad (8)$$

where n_t, ℓ_t and m_t are the quantum numbers. The final wavefunction is given by

$$\phi_f(\boldsymbol{\rho}) = \frac{1}{\sqrt{2}} \exp(-\rho/2) Y_{0,0}(\hat{\rho}) \equiv \tilde{R}_{1s}(\rho)\; Y_{0,0}(\hat{\rho}), \quad (9)$$

since the ground $1s$ state of the Ps atom is considered in the present work. The angle differential cross section (DCS) for the capture then reads

$$\left[\frac{d\sigma}{d\Omega}\right]_{n_t\ell_t m_t} = \frac{1}{4\pi^2}\,\frac{k_\beta}{k_i}\,\mu_\alpha\mu_\beta\,\left|T^-_{\alpha\beta}\right|^2, \quad (10)$$

where k_β is the magnitude of the Ps momentum.

Upon averaging equation (10) over m_t and denoting the electron occupancy number of the C_{60} $(n_t\ell_t)$ state by $\mathrm{occ}(n_t\ell_t)$, we obtain

$$\left[\frac{d\sigma}{d\Omega}\right]_{n_t\ell_t} = \frac{\mathrm{occ}(n_t\ell_t)}{2(2\ell_t+1)} \times \sum_{m_t}\left[\frac{d\sigma}{d\Omega}\right]_{n_t\ell_t m_t}. \quad (11)$$

The differential cross section in the forward direction, integrated from 0 to $\theta_{\rm max}$, is obtained as

$$[\sigma]_i^{[0,\theta_{\rm max}]} = \int_0^{\theta_{\rm max}} \sin(\theta)d\theta \int_0^{2\pi} d\varphi \left[\frac{d\sigma}{d\Omega}\right]_i, \quad (12)$$

where (θ,φ) are the angles of $\boldsymbol{k}_\beta$ (with respect to the incoming positron direction defined by $\boldsymbol{k}_i$ and which is considered to be along the z-axis). Finally, the angle-integrated cross section is evaluated as,

$$[\sigma]_{n_t\ell_t} = \int_0^{\pi} \sin(\theta)d\theta \int_0^{2\pi} d\varphi \left[\frac{d\sigma}{d\Omega}\right]_{n_t\ell_t}. \quad (13)$$

We should point out that the calculations of the narrow angular range differential results, equation (12), are more tedious compared to the angle-integrated cross sections, equation (13). Indeed, the analytic expression of the latter simplifies a lot due to the use of closure relations (see Eq. (25) in Ref. [29]). Furthermore, higher number of partial waves must be included in order to achieve the convergence of equation (12).

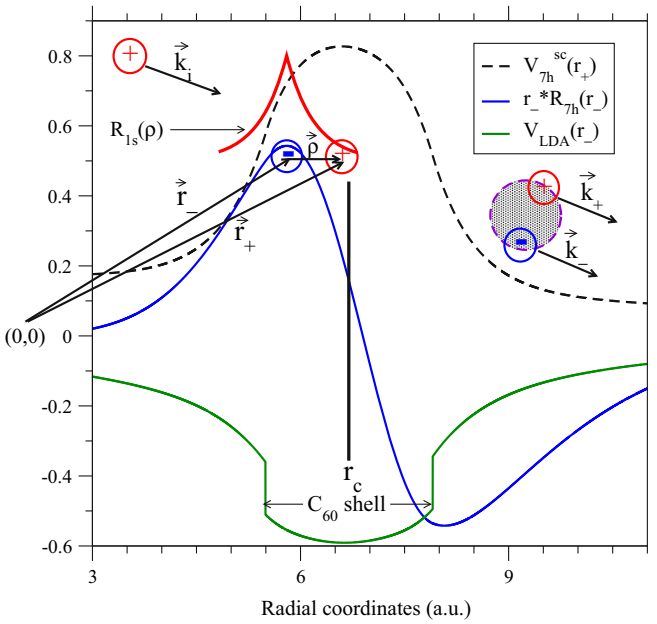

Fig. 1. The scattering potential $V_{7h}^{\rm sc}$ of the positron from C_{60}^+ after a $7h$ (HOMO) electron is captured, the radial HOMO wavefunction and the free C_{60} ground state LDA radial potential identifying the shell width around the C_{60} radius r_c. The position vectors, from the C_{60} center (0,0) roughly placed in the figure, and momentum vectors (for capture in the forward direction) are shown schematically. The Ps($1s$) radial wavefunction is also schematically shown.

3 Results and discussion

3.1 Scattering versus pairing effects

Our numerical calculations of fullerene state selected Ps($1s$) formation cross sections predicted trains of diffraction resonances as a function of the positron impact energy [27,29]. A simplified analytic model was proposed in reference [27] to explain the diffraction effect in the recoil momentum scale. The model assumes plane waves in equations (4) and (5) as well as dominant Ps formations in the forward direction. The model recognizes the following: (i) the shape of the Ps($1s$) radial wavefunction $\tilde{R}_{1s}(\rho)$ in equation (9) as a function of $\rho = |\boldsymbol{r}_+ - \boldsymbol{r}_-|$, shown schematically in Figure 1, ensures the maximum Ps probability density at $r_- = r_+$. (ii) The radial wave function of a fullerene ith level (Fig. 1) guarantees that the electron to form Ps is available closely around the shell. However, while the large values of $V_i^{\rm sc}$ (Fig. 1) at the molecular shell imply that the shell is a localized zone of the positron scattering by C_{60}^+, the long range Coulomb-like positron-electron pairing potential, $1/\rho$, is characteristically more diffused. Indeed, considering only the positron scattering potential $V_i^{\rm sc}$ in equation (5), the product $R_{1s}(\rho)V_i^{\rm sc}(r_-)$ $[r_+R_{7h}(r_-)]$ in the amplitude, equation (4), enhances localized Ps formation to yield strong diffraction effects in this model. On the other hand, if only the $1/\rho$ term is chosen in equation (5), the localization, and hence the diffraction effect, should somewhat weaken due to the diffused nature of $1/\rho$. Consequently, in the latter case, Ps

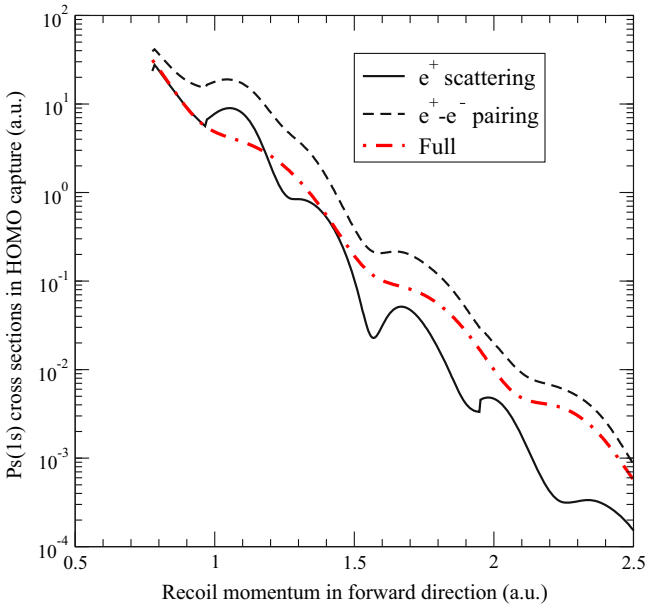

Fig. 2. Ps(1s) formation branching cross sections as a function of the recoil momentum in the forward direction by choosing the positron scattering and the positron-electron pairing components in equation (5) separately. The full cross section is also shown for comparison.

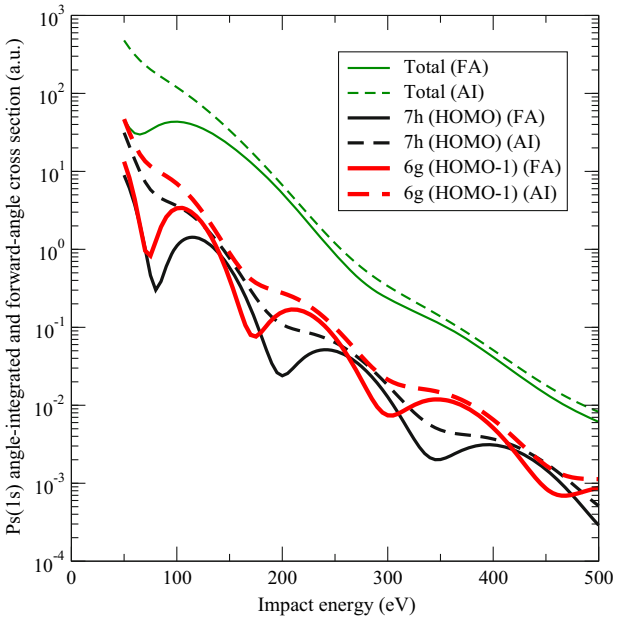

Fig. 3. Ps(1s) formation cross sections as a function of positron impact energy for the electron capture from C_{60} HOMO and HOMO-1 states. Both the 10° forward-angle (FA) and the angle-integrated (AI) results are shown. Total cross sections, summing over all target levels, are also presented in FA and IA schemes.

formation over somewhat wider radial region, due to contributions to the matrix element from a wider r-range, should increase the average strength of the cross section. In both cases, $R_{1s}(\rho)$ engenders a dephasing effect that simplifies the fringe pattern as the positron swings by the target [27].

Since these bright fringes (peaks) appear in the energy (momentum) domain, they are characteristically diffraction resonances. Angle-integrated branching cross section equation (13) for C_{60} HOMO capture calculated only choosing $V_i^{\rm sc}$ is presented in Figure 2 which, as anticipated in the above discussions, shows pronounced resonances. In contrast, the branching result in Figure 2 for pairing by only choosing $1/\rho$ exhibits decreased resolution of the resonance structures while the strength of the cross section is relatively higher as predicted. However, we must note, the full cross section, also shown in Figure 2, will include the contribution of the interference between these branches from their coherence. As further evident, while at lower recoil momenta the strength of the full cross section is drawn from the scattering branch, the strength gradually drifts toward the pairing branch with the increase of the momentum.

3.2 Forward angle cross sections

The success of an analytic model based on forward emissions [27] already suggests that the resonant effect is likely dominant in the forward direction of Ps formation. Let us approximate the three distorted waves in equations (4) and (5) as plane waves of the form $F_{\boldsymbol{k}}^{(\pm)}(\boldsymbol{r}) \sim \exp(i\boldsymbol{k}\cdot\boldsymbol{r})$. These plane waves can expand in spherical harmonics:

$$\exp(i\boldsymbol{k}\cdot\boldsymbol{r}) \sim \sum_{\ell,m} i^l j_\ell(kr) Y_{\ell,m}(\hat{k}) Y^*_{\ell,m}(\hat{r}). \tag{14}$$

With these and for the capture in Ps(1s) state, equations (4) and (5) simplify as

$$\begin{aligned} T^-_{\alpha\beta}(\boldsymbol{k}_i) \sim \sum_{\ell',m'} (-i)^{\ell'} \int dr_- r_-^2 j_{\ell'}(k_- r_-) R_{n_t\ell_t}(r_-) \\ \times \int d\hat{r}_- Y^*_{\ell_t,m_t}(\hat{r}_-) Y_{\ell',m'}(\hat{r}_-) W(\boldsymbol{r}_-;\boldsymbol{k}_i) \\ \times Y_{\ell',m'}(\hat{k}_-) \end{aligned} \tag{15}$$

and

$$\begin{aligned} W(\boldsymbol{r}_-;\boldsymbol{k}_i) \sim \sum_{\ell,m} (i)^\ell \int dr_+ r_+^2 j_\ell(qr_+) \left[V_i^{\rm sc}(r_+) - \frac{1}{\rho}\right] \\ \times \int d\hat{r}_+ \tilde{R}_{1s}(\rho) Y^*_{\ell,m}(\hat{r}_+) \\ \times Y_{\ell,m}(\hat{q}), \end{aligned} \tag{16}$$

where $\boldsymbol{q} = \boldsymbol{k}_+ - \boldsymbol{k}_i$ is the momentum transfer vector. If we now assume Ps formations in the forward direction so that $\hat{r}_-$ and $\hat{r}_+$ are identical and thus $\boldsymbol{\rho}$ is independent of $\hat{r}_+$, then the bare bone, that is the most pronounced possible, diffraction resonances will be given by equation (13). This is because $\theta = 0$ is the only contributing direction here. This is the basis of the analytic model mentioned above. However, the full numerical result of equation (13) includes contributions of all directions from the target.

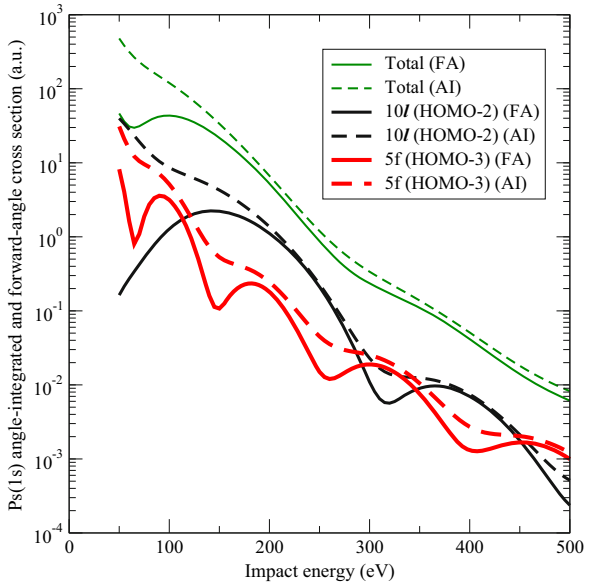

Fig. 4. Same as Figure 3 but for the capture from C_{60} HOMO-2 and HOMO-3 states.

This may introduce slight off-sets of the resonance locations in energy due to changes in $\boldsymbol{q}$ and, therefore in the recoil momentum, as the Ps emerging direction gradually deflects from $\theta = 0$ which may result in significant blur in the resonance structures.

The feature discussed above is, in essence, seen for HOMO, HOMO-1 captures (Fig. 3) and HOMO-2, HOMO-3 captures (Fig. 4). Each figure compares the forward angle (FA) results, obtained by integrating equation (12) for a rather narrow $\theta_{\max} = 10°$, with the fully angle-integrated (AI) results, equation (13), as a function of positron impact energy. All FA curves generally show more resolved resonances, versus AI curves, with much deeper minima between the resonances. This is because, within such a narrow forward cone, a very small variation of $\boldsymbol{q}$ does not allow much smearing of the sharpness of the naked forward-angle structures discussed above. But for AI results this smearing effect must be stronger. FA measurements, therefore, is of an obvious benefit for experimental access to the resonances. One may also note that all FA cross sections have weaker non-resonant background strength at smaller impact energies, while they quickly catch up with the AI strength with increasing impact energy. This behavior is very similar for HOMO, HOMO-1 and HOMO-3 captures where all these C_{60} levels are of π character. For HOMO-2 (Fig. 4), which is a σ level on the other hand, while the lower energy difference is dramatic, the strength of FA closes in that of IA rather rapidly with increasing energy. This general trend is not surprising since one expects dominant contribution increasingly from forward directions of Ps formation with higher impact energies. This also automatically implies that the sharpness of the resonances in FA scheme is higher at lower-energy impacts, as evident in the results.

The curve is very flat at the level of the total cross section which sums over all capture levels. This is due to the random energy off-sets of resonance positions for captures from various levels with different electronic binding energies. As Figures 3 and 4 also indicate, even in the FA scheme of the total cross section the result does not improve enough in resolving the structures, except at the very lowest energies. Therefore, capture state specific forward-angle measurements promises to be the best option to experimentally measure these resonances.

4 Conclusion

In conclusion, we present the results of cross section of Ps formation within a narrow forward angle in the positron impact on C_{60}. The C_{60} ground state structures are modeled by a simple but successful LDA methodology that used LB exchange-correlation functional. The positron scattering process, on the other hand, uses a distorted wave framework. The diffraction driven resonances are found to be more pronounced in the forward direction, while the non-resonant background of the cross section does not loose much of its strength. This outcome may generate further motivation to measure the resonances in Ps formation spectroscopy whose current laboratory techniques may find the angle-resolved measurements more amenable. Even though for the current study a 10° angle around the forward direction is chosen, calculations for even narrower angles can be made if required to match experimental abilities.

One may, however, wonder if the oven temperature of about 800 K to produce C_{60} vapor would wash out the resonances. We do not believe this is a hindrance because of the following reason. Temperature can affect by: (i) coupling of the electronic-modes with the temperature-induced phonon-modes of the ion core [46] and (ii) fluctuations of the C_{60} shape around its absolute-zero temperature shape [47]. However, previous photoionization calculations [48] showed that it needed a convolution of the results to add a width less than 1 eV to compare with measurements of gas phase C_{60}. In comparison with energy separations of more than 100 eV between resonances in Figures 3 and 4, this width is rather too tiny. In addition, the HOMO-LUMO energy gap of C_{60} is around 1.5 eV which corresponds to about 17 000 K which is much greater than the 800 K. Therefore, thermal vibrations is not expected to affect the population of the electronic states to destroy the diffraction structures.

Nanoparticles, including fullerenes, are attractive in both experimental and theoretical spectroscopic research. Fullerenes can nowadays be injected in the collision chamber in gas-phase [49]. Also, such diffraction effects studied in this paper, which began with our earlier published research [27–29], in Ps formation should be universal for other nanosystems as well. These may include metal clusters, carbon nanotubes, or even quantum dots, all of which contain parcels of delocalized electron gas. Therefore, exploring possibilities of Ps generation spectroscopy for a selected capture state of C_{60} and within a selected narrow angular range along the forward direction may come a long way to expand this research for other systems.

The research is supported by the National Science Foundation Grant No. PHY-1806206, USA.

Author contribution statement

PAH and HSC contributed to the conception, design and implementation of the research, to the computation and analysis of the results, and to the writing of the manuscript.

References

1. G. Laricchia, S. Armitage, Á. Kövér, Adv. At. Mol. Opt. Phys. **56**, 1 (2008)
2. P.J. Schultz, K.G. Lynn, Rev. Mod. Phys. **60**, 701 (1988)
3. D.G. Green, G.F. Gribakin, Phys. Rev. Lett. **114**, 093201 (2015)
4. N. Prantzos, C. Boehm, A.M. Bykov, R. Diehl, K. Ferrière, N. Guessoum, P. Jean, J. Knoedlseder, A. Marcowith, I.V. Moskalenko, A. Strong, G. Weidenspointner, Rev. Mod. Phys. **83**, 1001 (2011)
5. T. Kavetskyy, V. Tsmots, A. Kinomura, Y. Kobayashi, R. Suzuki, H.F.M. Mohamed, O. Sausa, V. Nuzhdin, V. Valeev, A.L. Stepanov, J. Phys. Chem. B **118**, 4194 (2014)
6. A.W. Dong, C. Fong, L.J. Waddington, A.J. Hill, B.J. Boyd, C.J. Drummond, Phys. Chem. Chem. Phys. **17**, 1705 (2015)
7. P. Pérez, D. Banerjee, F. Biraben et al., Hyperfine Interact. **233**, 21 (2015)
8. D.B. Cassidy, A.P. Mills, Jr., Nature **449**, 195 (2007)
9. R. Ferragut, A. Calloni, A. Dupasquier, G. Consolati, F. Quasso, M.G. Giammarchi, D. Trezzi, W. Egger, L. Ravelli, M.P. Petkov, S.M. Jones, B. Wang, O.M. Yaghi, B. Jasinska, N. Chiodini, A. Paleari, J. Phys. Conf. Ser. **225**, 012007 (2010)
10. O. Morandi, P.A. Hervieux, G. Manfredi, Phys. Rev. A **89**, 033609 (2014)
11. K. Shu, X. Fan, T. Yamazak, T. Namba, S. Asai, K. Yoshioka, M. Kuwata-Gonokami, J. Phys. B **49**, 104001 (2016)
12. D.B. Cassidy, A.P. Mills, Jr., Phys. Rev. Lett. **100**, 013401 (2008)
13. S.G. Karshenboim, Int. J. Mod. Phys. A **19**, 3879 (2004)
14. C.M. Surko, M. Leventhal, A. Passner, Phys. Rev. Lett. **62** 901 (1989)
15. J.R. Machacek, F. Blanco, G. Garcia, S.J. Buckman, J.P. Sullivan, J. Phys. B **49**, 064003 (2016)
16. O. Sueoka, M.K. Kawada, M. Kimura, Nucl. Instrum. Methods Phys. Res. B **171**, 96 (2000)
17. M. Eldrup, A. Vehanen, P.J. Schultz, K.G. Lynn, Phys. Rev. Lett. **51**, 2007 (1983)
18. C.L. Wang, K. Hirata, J. Kawahara, Y. Kobayashi, Phys. Rev. B **58**, 14864 (1998)
19. A. Cabral-Prietoa, I. García-Sosaa, R. López-Castañaresb, O. Olea-Cardosob, Micropor. Mesopor. Mater. **175**, 134 (2013)
20. B.S. Cooper, A.M. Alonso, A. Deller, L. Liszkay, D.B. Cassidy, Phys. Rev. B **93**, 125305 (2016)
21. A.C.L. Jones, H.J. Rutbeck-Goldman, T.H. Hisakado, A.M. Piñeiro, H.W.K. Tom, A.P. Mills, Jr., B. Barbiellini, J. Kuriplach, Phys. Rev. Lett. **117**, 216402 (2016)
22. P. Crivelli, D. Cooke, B. Barbiellini, B.L. Brown, J.I. Feldblyum, P. Guo, D.W. Gidley, L. Gerchow, A.J. Matzger, Phys. Rev. B **89**, 241103(R) (2014)
23. A.C.L. Jones, H.J. Goldman, Q. Zhai, P. Feng, H.W.K. Tom, A.P. Mills, Phys. Rev. Lett. **114**, 153201 (2015)
24. S.L. Andersen, D.B. Cassidy, J. Chevallier, B.S. Cooper, A. Deller, T.E. Wall, U.I. Uggerhoj, J. Phys. B **49**, 204003 (2016)
25. A.C.L. Jones, T.H. Hisakado, H.J. Goldman, H.W.K. Tom, A.P. Mills, Jr., D.B. Cassidy, Phys. Rev. A **90**, 012503 (2014)
26. R. McConnell, G. Gabrielse, W.S. Kolthammer, P. Richerme, A. Müllers, J. Walz, D. Grzonka, M. Zielinski, D. Fitzakerley, M.C. George, J. Phys. B **49**, 064002 (2016)
27. P.A. Hervieux, A.R. Chakraborty, H.S. Chakraborty, Phys. Rev. A **95**, 020701(R) (2017)
28. H.S. Chakraborty, A.R. Chakraborty, P.A. Hervieux, J. Phys. Conf. Ser. **875**, 042701 (2019)
29. P.A. Hervieux, A.R. Chakraborty, H.S. Chakraborty, Phys. Rev. A **100**, 020701(R) (2017)
30. E.K. Anderson, R.A. Boadle, J.R. Machacek, L. Chiari, C. Makochekanwa, S.J. Buckman, M.J. Brunger, G. Garcia, F. Blanco, O. Ingolfsson, J.P. Sullivan, J. Chem. Phys. **141**, 034306 (2014)
31. M. Shipman, S. Armitage, J. Beale, S.J. Brawley, S.E. Fayer, A.J. Garner, D.E. Leslie, P. Van Reeth, G. Laricchia, Phys. Rev. Lett. **115**, 033401 (2015)
32. T. Falke, W. Raith, M. Weber, U. Wesskamp, J. Phys. B **28**, L505 (1995)
33. M.J. Puska, R.M. Nieminen, Phys. Rev. A **47**, 1181 (1993)
34. J. de Vries, H. Steger, B. Kamke, C. Menzel, B. Weisser, W. Kamke, I.V. Hertel, Chem. Phys. Lett. **188**, 159 (1992)
35. O. Gunnarsson, B. Lundqvist, Phys. Rev. B **13**, 4274 (1976); Erratum: Phys. Rev. B **15**, 6006 (1977)
36. R. van Leeuwen, E.J. Baerends, Phys. Rev. A **49**, 2421 (1994)
37. G.L. Oliver, J.P. Perdew, Phys. Rev. A **20**, 397 (1979)
38. N. Troullier, J.L. Martins, Phys. Rev. B **46**, 1754 (1992)
39. J.H. Weaver, J.L. Martins, T. Komeda, Y. Chen, T.R. Ohno, G.H. Kroll, N. Troullier, Phys. Rev. Lett. **66**, 1741 (1991)
40. M. Vos, S.A. Canney, I.E. McCarthy, S. Utteridge, M.T. Michalewicz, E. Weigold, Phys. Rev. B **56**, 1309 (1997)
41. J. Choi, E.H. Chang, D.M. Anstine, M.E. Madjet, H.S. Chakraborty, Phys. Rev. A **95**, 023404 (2017)
42. S.W.J. Scully, E.D. Emmons, M.F. Gharaibeh, R.A. Phaneuf, A.L.D. Kilcoyne, A.S. Schlachter, S. Schippers, A. Müller, H.S. Chakraborty, M.E. Madjet, J.M. Rost, Phys. Rev. Lett. **94**, 065503 (2005)
43. A. Rüdel, R. Hentges, U. Becker, H.S. Chakraborty, M.E. Madjet, J.M. Rost, Phys. Rev. Lett. **89**, 125503 (2002)
44. O.A. Fojón, R.D. Rivarola, R. Gayet, J. Hanssen, P.A. Hervieux, Phys. Rev. A **54**, 4923 (1996)
45. O.A. Fojón, R.D. Rivarola, J. Hanssen, P.A. Hervieux, J. Phys. B **34**, 4279 (2001)
46. G.F. Bertsch, D. Tománek, Phys. Rev. B **40**, 2749 (1989)
47. J.M. Pacheco, R.A. Broglia, Phys. Rev. Lett. **62**, 1400 (1989)
48. M.E. Madjet, H.S. Chakraborty, J.M. Rost, S.T. Manson, J. Phys. B **41**, 105101 (2008)
49. C.M. Thomas, K.K. Baral, N.B. Aryal, M. Habibi, D.A. Esteves-Macaluso, A.L.D. Kilcoyne, A. Aguilar, A.S. Schlachter, S. Schippers, A. Müller, R.A. Phaneuf, Phys. Rev. A **95**, 053412 (2017)